Cryo-EM analysis provides new mechanistic insight into ATP binding to Ca^{2+}-ATPase SERCA2b

Yuxia Zhang[1] [ID], Satoshi Watanabe[1] [ID], Akihisa Tsutsumi[2], Hiroshi Kadokura[1] [ID], Masahide Kikkawa[2] [ID] & Kenji Inaba[1,*] [ID]

Abstract

Sarco/endoplasmic reticulum Ca^{2+}-ATPase (SERCA) 2b is a ubiquitous SERCA family member that conducts Ca^{2+} uptake from the cytosol to the ER. Herein, we present a 3.3 Å resolution cryo-electron microscopy (cryo-EM) structure of human SERCA2b in the E1·2Ca^{2+} state, revealing a new conformation for Ca^{2+}-bound SERCA2b with a much closer arrangement of cytosolic domains than in the previously reported crystal structure of Ca^{2+}-bound SERCA1a. Multiple conformations generated by 3D classification of cryo-EM maps reflect the intrinsically dynamic nature of the cytosolic domains in this state. Notably, ATP binding residues of SERCA2b in the E1·2Ca^{2+} state are located at similar positions to those in the E1·2Ca^{2+}-ATP state; hence, the cryo-EM structure likely represents a preformed state immediately prior to ATP binding. Consistently, a SERCA2b mutant with an interdomain disulfide bridge that locks the closed cytosolic domain arrangement displayed significant autophosphorylation activity in the presence of Ca^{2+}. We propose a novel mechanism of ATP binding to SERCA2b.

Introduction

Sarco/endoplasmic reticulum Ca^{2+} ATPase (SERCA) proteins are members of the P-type ATPase superfamily that are involved in transporting various cations including protons, calcium, potassium, and sodium ions across cell membranes (Bublitz *et al*, 2010), and other physiological processes such as lipid flipping (Axelsen & Palmgren, 1998). In terms of structures and mechanisms of action, SERCAs are the best studied members of the superfamily (Møller *et al*, 2005; Michelangeli & East, 2011). About 20 years ago, the first crystal structure of SERCA1a, an isoform expressed specifically in fast-twitch skeletal-muscle fibers (Zhang *et al*, 1995), was reported

in the E1·2Ca^{2+} state (Toyoshima *et al*, 2000). Crystal structures of SERCA1a in different intermediate states have since been determined, providing deep insights into the underlying mechanism of Ca^{2+} transport by the Ca^{2+} ATPase (Fig 1A), as well as the general structural and mechanistic features of the P-type ATPase superfamily (Toyoshima, 2009; Bublitz *et al*, 2013; Dyla *et al*, 2019b).

Despite remarkable progress in structural and mechanistic studies on SERCA isoforms, their catalytic mechanisms remain contentious. While it is believed that the Ca^{2+} transport cycle of SERCA is initiated by the coordinated binding of two Ca^{2+} ions and one ATP molecule to the transmembrane (TM) and nucleotide-binding (N) domains, respectively (Mueller *et al*, 2004; Inesi *et al*, 2006; Toyoshima, 2009; Møller *et al*, 2010), one of the most discussed issues is the functional significance of the widely opened cytosolic domain arrangement observed in the crystal structure of SERCA1a in the E1·2Ca^{2+} state (Liu & Barth, 2003; Dyla *et al*, 2019b). Thus, it is still under debate as to whether such a gate opening accompanied by large domain movements actually takes place when the ATP molecule enters the ATP-binding pocket (Ravishankar *et al*, 2020). Based on the highly mobile nature of the actuator (A) and N domains in this state, and the possible bias caused by crystal packing, the crystal structure may represent only one structural aspect of the calcium-bound but ATP-unbound state. In this context, scientists have been seeking genuine and as-yet-unidentified SERCA intermediates, and visualizing their structures by employing various spectroscopic and computational methods, including fluorescence resonance energy transfer (FRET) (Dyla *et al*, 2017; Raguimova *et al*, 2018), molecular dynamics (MD) simulation (Mueller *et al*, 2004; Huang *et al*, 2009; Kekenes-Huskey *et al*, 2012; Das *et al*, 2014), and time-resolved X-ray solution scattering (TR-XSS) (Ravishankar *et al*, 2020). Recent TR-XSS analysis combined with MD simulations identified three transient states of SERCA1a during the transition to the ATP-bound state, named the pre-pulse (i.e., pre-ATP-bound), intermediate, and late states, with respect to the cytosolic domain arrangements (Ravishankar *et al*, 2020), although this approach did not provide high-resolution structures due to its inherent technical limitations.

In the present work, we employed cryo-EM single-particle analysis and thereby determined a new intermediate structure of human SERCA2b in the E1·2Ca^{2+} state at a resolution of 3.3 Å. We revealed

---

1 Institute of Multidisciplinary Research for Advanced Materials, Tohoku University, Sendai, Japan
2 Graduate School of Medicine, The University of Tokyo, Tokyo, Japan
*Corresponding author. Tel: +81 22 217 5604; Fax: +81 22 217 5605; E-mail: kenji.inaba.a1@tohoku.ac.jp
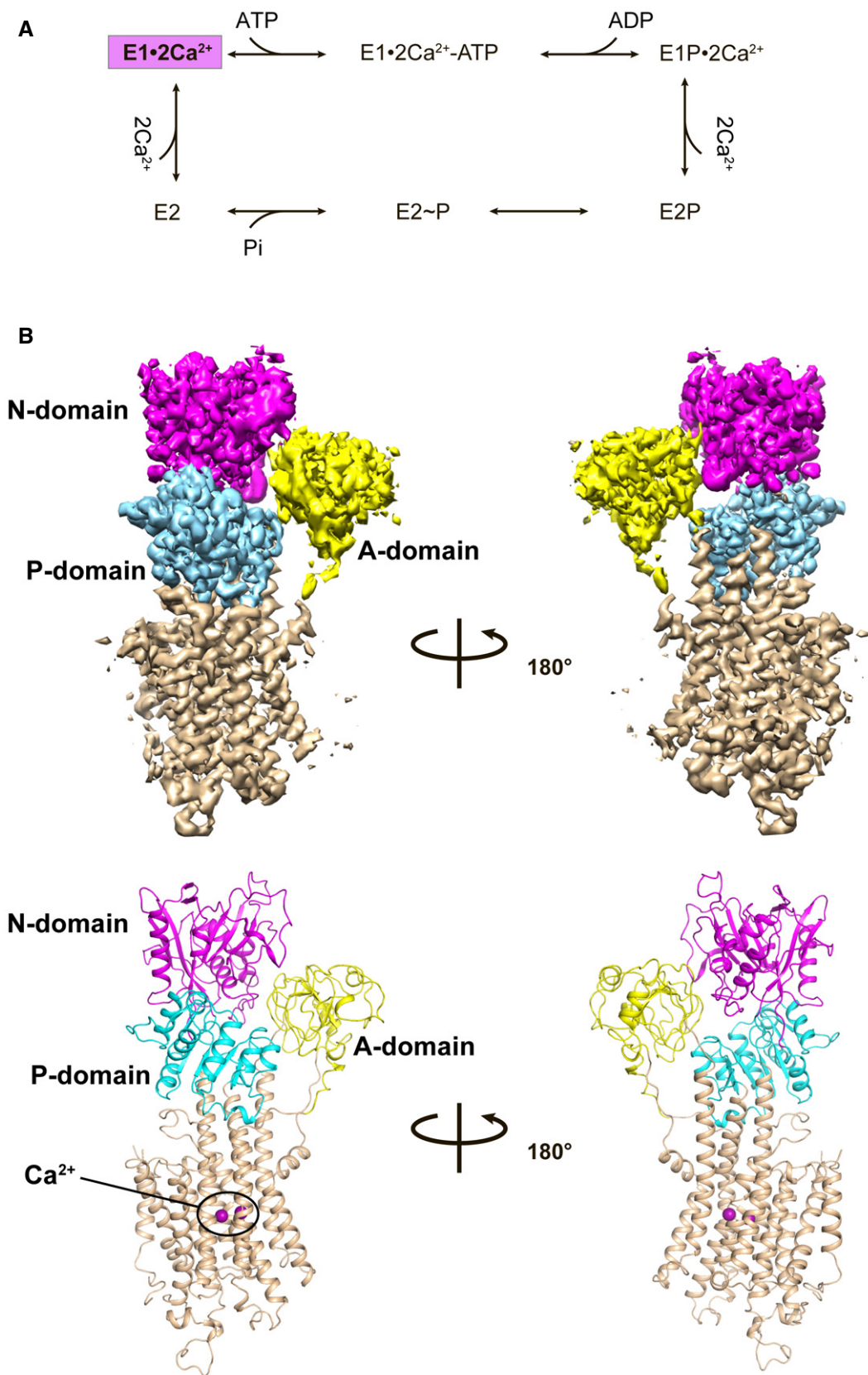
A

$$E1 \cdot 2Ca^{2+} \xrightarrow{\text{ATP}} E1 \cdot 2Ca^{2+}\text{-ATP} \longleftrightarrow E1P \cdot 2Ca^{2+}$$

2Ca²⁺ ... ADP ... 2Ca²⁺

$$E2 \xleftarrow{} E2{\sim}P \longleftrightarrow E2P$$

Pi

B

Figure 1.

Figure 1. Cryo-EM structure of SERCA2b WT in the E1·2Ca²⁺ state.

A Catalytic cycle for SERCA to transport Ca²⁺ from the cytosol to the ER lumen through ATP hydrolysis. The intermediate state of which cryo-EM structures have been determined in this work is colored magenta.

B Cryo-EM map of SERCA2b WT in the E1·2Ca²⁺ state (upper) and its cartoon representation (lower). The A, N, and P domains and transmembrane helices (TM1—TM11) are colored yellow, magenta, cyan, and wheat, respectively.

that a significant portion of SERCA2b in this state adopts a much more closed cytosolic domain arrangement than observed in previous crystal structures of SERCA1a (Toyoshima *et al*, 2000). Interestingly, the cryo-EM structure is highly similar to our previously reported cryo-EM structure of SERCA2b in the E1·2Ca²⁺-AMPPCP state (Zhang *et al*, 2020), in terms of both the TM helix arrangement and the location and orientation of ATP-binding residues. In this conformation, SERCA2b in the E1·2Ca²⁺ state possesses a compact headpiece cluster of the cytosolic domains, forming a cavity that appears primed for ATP binding. In line with these structural findings, a SERCA2b mutant with an interdomain disulfide bridge that locks the relative positions of the A and N domains in the closed form displayed significant autophosphorylation activity, suggesting that the newly identified structure represents a preformed state immediately prior to ATP binding. Based on these results, we propose a new mechanism of ATP binding to Ca²⁺-bound SERCA2b and discuss the ligand-induced conformational transitions in SERCA during its catalytic cycle.

Results

SERCA2b displays multiple conformations in the E1·2Ca²⁺ state

We expressed and purified SERCA2b essentially as described previously (Inoue *et al*, 2019; Zhang *et al*, 2020). The cryo-EM structure of SERCA2b in the E1·2Ca²⁺ state was determined at a resolution of 3.3 Å (Fig 1 and Table EV1). In the first round of 3D classification based on selected 2D classification images, cryo-EM maps of Ca²⁺-bound SERCA2b were classified into four different classes (Fig EV1A). The additional round of 3D classification generated two major classes of conformations named "closed form" and "possible open form" in significant abundance (~20.7 and 37.7%, respectively; Fig EV1A). The "possible-open-form" cryo-EM maps roughly superpose with the crystal structure of SERCA1a in the E1·2Ca²⁺ state (PDB ID: 1SU4 and 2C9M) (Toyoshima *et al*, 2000; Jensen *et al*, 2006) (Fig EV1C), suggesting that SERCA2b actually adopts the previously reported "open form" in the presence of Ca²⁺. However, the resolution of the "possible-open-form" cryo-EM map was low (~12 Å resolution), and not improved by additional 3D classifications, probably due to the highly mobile cytosolic domains or the ensemble of their heterogeneous arrangements in this state. Alternatively, it is possible that such low-resolution cryo-EM maps may be ascribed to particle damage during grid preparation and/or data collection, resulting in inaccurate averaged particle densities.

Importantly, the closed form identified by the present cryo-EM analysis places three cytosolic domains in much closer proximity than the open form (Figs 1B and 2). The presence of four similar cryo-EM maps (Fig EV1A) suggests that the closed form is less diverse in cytosolic domain arrangement or fluctuates to a lesser

extent than the open form. In this context, a pre-ATP-bound form had been identified by unrestrained MD simulations from the "open-form" crystal structure of SERCA1a (Ravishankar *et al*, 2020), during which the A and N domains were calculated to approach each other, with the distance of 45 Å between Thr171 (A domain) and Lys515 (N domain) decreasing to 29 Å. Eventually, these domains were settled at the intermediate positions between those in the present "closed-form" cryo-EM structure of SERCA2b and those in the "open-form" crystal structure of SERCA1a.

Overall cryo-EM structure of the closed form in the E1·2Ca²⁺ state

In the present "closed-form" cryo-EM map of SERCA2b in the E1·2Ca²⁺ state, all cytosolic domains and TM helices, including TM11 and the luminal extension tail (LE), can be clearly seen (Figs 1B, EV2A and EV5). Similar to E1·2Ca²⁺-AMPPCP and E2-BeF₃⁻ states (Zhang *et al*, 2020), the LE in the E1·2Ca²⁺ state is located near the luminal ends of TM10 and TM7, and approaches the short α-helix (Phe866—Ser870) in L7/8 (Fig EV2A, bottom inset). The P domain displayed stronger density and higher resolution than the A and N domains (Fig EV1B), suggesting that it is relatively static in this state. By contrast, the A domain and the upper part of the N domain were not well-defined and yielded fragmented density, resulting in a lower resolution (~4.5 Å) than other domains (Fig EV1B). The density of two Ca²⁺ ions bound in the pocket formed by TM4, 5, 6, and 8 is present at almost the same position as in the crystal structure of SERCA1a in the E1·2Ca²⁺ state (Fig EV2B and D) and the cryo-EM structure of SERCA2b in the E1·2Ca²⁺-AMPPCP state (Fig EV2C) (Zhang *et al*, 2020).
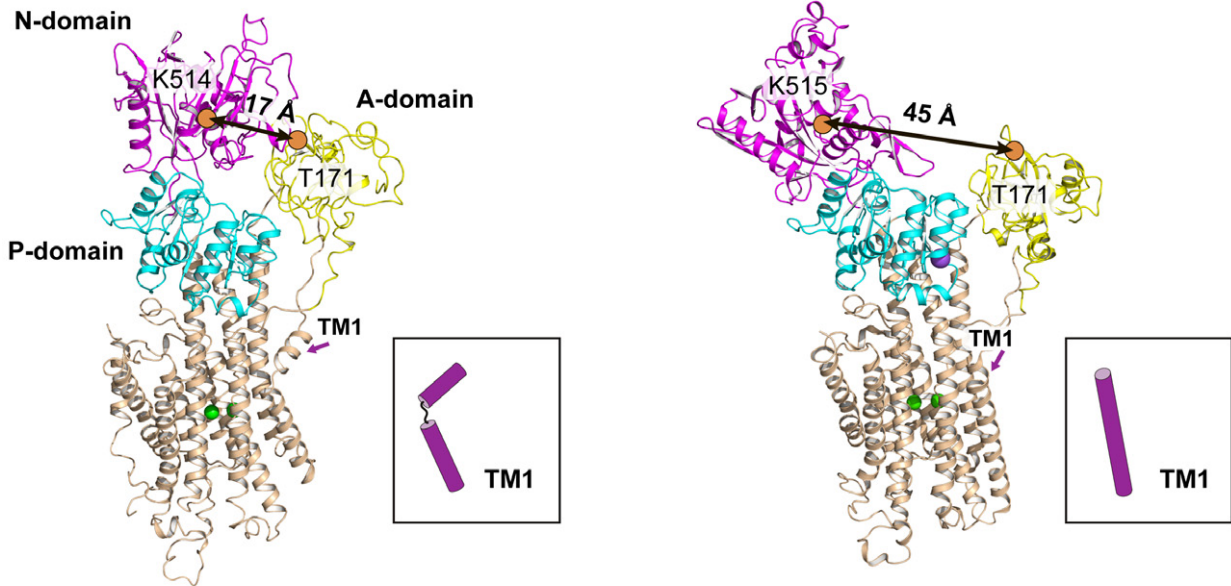
Structural comparison between the closed and open forms in the E1·2Ca²⁺ state

The overall domain arrangement in the "closed-form" cryo-EM structure of SERCA2b differs significantly from that in the "open-form" crystal structure of SERCA1a (Toyoshima *et al*, 2000), with a root mean square deviation (RMSD) value of 5.9 Å for all Cα atoms (Fig 2A). Meanwhile, the TM helices undergo small positional shifts between the open and closed forms, with an RMSD value of 0.83 Å for TM1—TM10. Thus, the positions and orientations of TM helices seem to be stabilized by bound Ca²⁺. However, among all TM helices, TM1 and TM2 undergo a remarkable movement (Fig 2A and C). TM2 moves upward and shifts away from TM3 (Fig 2C). Similarly, TM1 moves toward the cytosolic side. Notably, the cytosolic part of TM1 is kinked largely at Asp59 in the closed form, so that it becomes nearly parallel to the membrane surface (Fig 2A and C). The kink of TM1 is believed to function as a "sliding door" allowing Ca²⁺ entry and thereby facilitating Ca²⁺ binding in SERCA proteins (Winther *et al*, 2013). Such a kink in the N-terminal TM

A

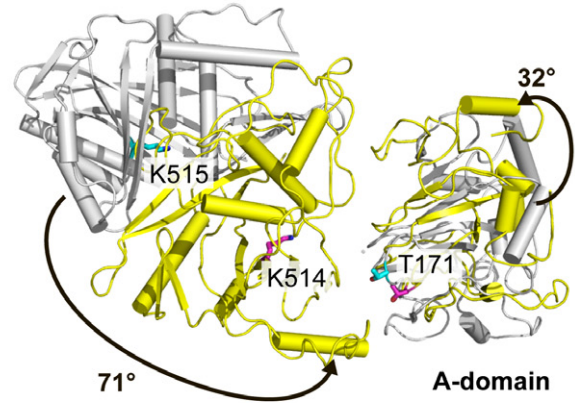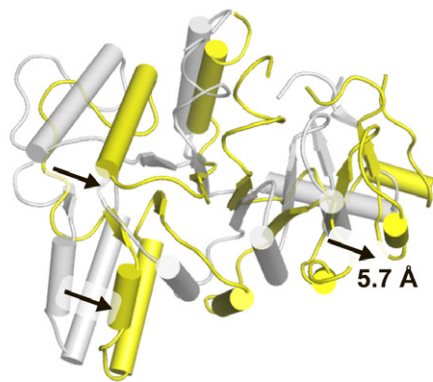**cryo-EM structure of SERCA2b in E1·2Ca²⁺ state (closed form)**

crystal structure of SERCA1a in E1·2Ca²⁺ state (open form)
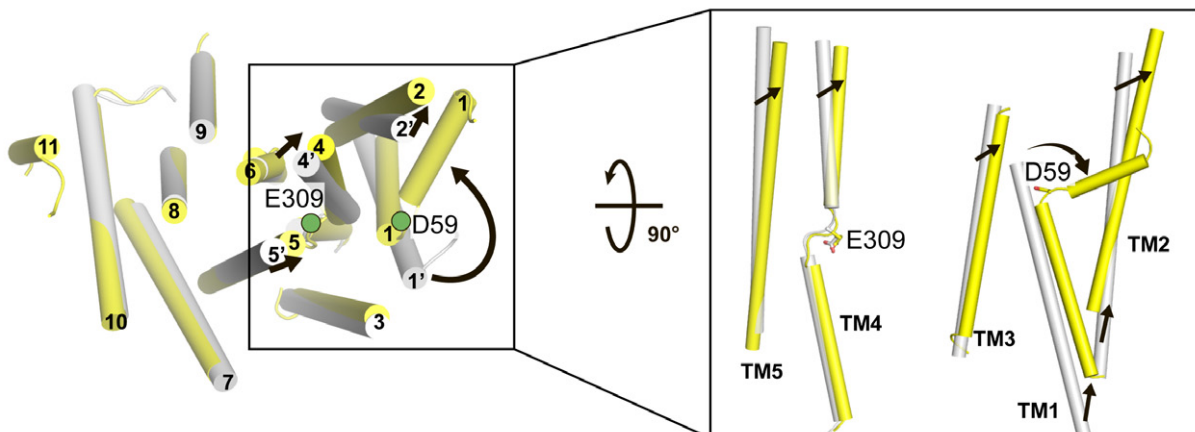

B

C

Figure 2.

◀

Figure 2.   Comparison between a "closed-form" cryo-EM structure of SERCA2b and an "open-form" crystal structure of SERCA1a in the E1·2Ca²⁺ state.

A   Cryo-EM structure of SERCA2b WT in the $E1 \cdot 2Ca^{2+}$ state (left) and the crystal structure of SERCA1a (PDB ID: 1SU4) in the $E1 \cdot 2Ca^{2+}$ state (right). The A, N, and P domains are colored yellow, magenta, and cyan, respectively. TM helices are colored wheat. TM1 in these two structures is highlighted by cartoons on the right of ribbon diagrams. Calcium ions are represented as green spheres. Orange circles indicate Thr171 and Lys514 (Lys515 in SERCA1a), and the double-headed arrows in black represent the distance between these two residues.

B   Top view of the P domain (left), the N and A domains (right) in the cryo-EM structure of SERCA2b (yellow), and the crystal structure of SERCA1a in the $E1 \cdot 2Ca^{2+}$ state (gray). The rearrangements of these cytosolic domains are indicated by black arrows.

C   Top view of the TM helix domain (left) in the cryo-EM structure of SERCA2b (yellow) and the crystal structure of SERCA1a (gray) in the $E1 \cdot 2Ca^{2+}$ state. The right inset highlights the rearrangements of TM1–TM5 between these two structures. Structures are superimposed such that the RMSD of Cα atoms in TM7 to TM10 is minimized. The green circles represent Asp59 and Glu309 located at the kink sites of TM1 and TM4, respectively.

helix is commonly seen in P-type ATPases of known structure (Dyla *et al*, 2017; Focht *et al*, 2017), including P4-type ATPase (Hiraizumi *et al*, 2019; Timcenko *et al*, 2019), and Na⁺/K⁺-ATPase (Morth *et al*, 2007; Nyblom *et al*, 2013). Concomitant with the movements of TM1 and TM2, the A domain undergoes a significant positional shift (8.8 Å) and rotation (32°) (Fig 2B, right).

Compared with TM1 and TM2, TM4 and TM5 seem to undergo smaller positional shifts between the open and closed forms (Fig 2C). However, their cytosolic halves, which are located distant from the Ca²⁺-binding sites and directly linked to the P domain, are bent toward TM2 by 20.7° and 6.9°, respectively, in the closed form (Fig 2C, inset). Concomitantly, the P domain rotates by 12° and approaches the A domain by 5.7 Å relative to that in the open form (Fig 2B, left). As a result, the side chain of Asn213 in the A domain is hydrogen bonded to the side chain of Thr723 in the P domain (Fig 4A, left inset), stabilizing the closed form in the E1·2Ca²⁺ state.

Of note, the position of the N domain in the closed form is largely different from that in the "open-form" crystal structure of SERCA1a (Figs 2A and B, right); the distance between Cα atoms of Lys515 (N domain) and Thr171 (A domain) is 17 Å in the former, but 45 Å in the latter. In the closed form, the close proximity of the N domain to the A domain seems to be ensured by five side-chain interactions between these two domains: Arg134 (A domain)– Asp426 (N domain), Arg139 (A domain)–Glu435 (N domain), Arg139 (A domain)–Lys436 (N domain), Thr171 (A domain)– Glu486 (N domain), and Lys218 (A domain)–Asp422 (N domain) (Fig 4A, right inset). Thus, although the N domain was previously shown to undergo a large movement upon ATP binding to hold the nucleotide tightly (Toyoshima & Mizutani, 2004), the present cryo-EM analysis suggests that such an extensive domain movement can occur within the E1·2Ca²⁺ state even without ATP binding, hence the closed form accounts for a significant proportion of the population in this state.

Structural comparison between the closed form of the E1·2Ca²⁺ state and the E1·2Ca²⁺-AMPPCP state

We next compared the "closed-form" cryo-EM structure of SERCA2b in the E1·2Ca²⁺ state with that of SERCA2b in the E1·2Ca²⁺-AMPPCP state, in which the cytosolic domains are in even closer contact with each other due to bound AMPPCP (Fig 3) (Zhang *et al*, 2020). Although both structures possess a closed headpiece cluster of the cytosolic domains, they show significant differences, especially in the position of the cytosolic domains, with an RMSD value of 3.6 Å for all Cα atoms (Fig 3B). By contrast, structural alignment based on

TM7–TM10 demonstrated that all TM helices including the Ca²⁺-binding sites are highly superimposable with each other between E1·2Ca²⁺ and E1·2Ca²⁺-AMPPCP states, with an RMSD value of 0.197 Å (Fig 3B, bottom inset). Thus, TM helices barely move during the transition from the "closed-form" SERCA2b in the E1·2Ca²⁺ state to the E1·2Ca²⁺-ATP state.

Among the three cytosolic domains, the N domain moves most prominently during the transition from E1·2Ca²⁺ to E1·2Ca²⁺-ATP states, with rotation of 16° (Fig 3A, middle). Consequently, the N domain approaches the P domain, leading to tight ATP binding. Concomitant with the N domain movement, the P domain undergoes ATP-induced conformational changes; the C-terminal half of the P domain, including three β-strands and three α-helices, inclines toward the phosphorylation site (Asp351) upon ATP binding (Fig. 3A, right), forming an even more compact globular fold, as was also seen in crystal structure of SERCA2a in the E2-AMPPCP state (Kabashima *et al*, 2020). Thus, the P domain folds loosely in the closed form of the E1·2Ca²⁺ state, which may serve to facilitate the delivery of the γ-phosphate group of ATP into the appropriate site in the P domain. The A domain also undergoes positional shifts upon ATP binding, with rotation of 14° (Fig 3A, left), leading to tighter interactions with the N and P domains, as described in the following paragraph.

In brief, the cytosolic headpiece cluster of SERCA2b becomes even more compact upon ATP binding. In support of this, multiple salt bridges and hydrogen bonds are formed at the cytosolic domain interfaces in the E1·2Ca²⁺-ATP state, including those between the A and N domains: Arg134 (A domain)–Asp426 (N domain), Arg134 (A domain)–Tyr427 (N domain), Arg139 (A domain)–Lys436 (N domain), Thr171 (A domain)–Glu486 (N domain), Lys218 (A domain)–Asp422 (N domain), Thr171 (A domain)–Leu577 (N domain), Arg139 (A domain)–Glu435 (N domain), and Lys169 (A domain)–Thr484 (N domain) (Fig 4B, right inset), and those between the A and P domains: Gly156 (A domain)–Thr723 (P domain), Asn213 (A domain)–Thr728 (P domain), and Asn213 (A domain)–Thr723 (P domain) (Fig 4B, left inset).

Notably, many of the above interactions are already formed prior to ATP binding, between the A and N domains and between the A and P domains (Fig 4A, left and right insets). Additionally, hydrogen bonds are newly identified between the side chain of Arg489 (N domain) and the main-chain carbonyl group of Val678 (P domain) and between the side chains of Lys492 (N domain) and Arg677 (P domain) in the E1·2Ca²⁺ state (Fig 4A, left inset). As a consequence of these interdomain interactions, the ATP binding residues, namely, Asp351, Met494, Glu442, Phe482, Arg489, Lys514, Arg559, Lys683, Arg677, Asp702, and Asn705, in the E1·2Ca²⁺ state are

located at similar positions to those in the E1·2Ca^{2+}-ATP state, and the cavity constituted by these residues appears to shrink upon ATP binding (Fig 3B, right inset, and Fig EV2E). In this regard, the "closed-form" E1·2Ca^{2+} state newly identified in this study can be interpreted as a preformed state of SERCA immediately prior to ATP binding.

ATP enters and phosphorylates the closed form of SERCA2b

To examine whether the "closed-form" SERCA2b in the E1·2Ca^{2+} state does allow ATP to enter the cavity, we carried out biochemical experiments. With the purpose of locking the relative positions of the A and N domains in the closed form (Lopez-Redondo et al, 2018), we focused upon the interface between the A and N domains and found several amino acid pairs that have potential to form an interdomain disulfide bridge. We thus prepared six kinds of SERCA2b mutants by site-directed mutagenesis: Q138C/D426C, V137C/D426C, A154C/G438C, V155C/G438C, T171C/E486C, and T171C/L577C (Fig EV3A). Among them, T171C/L577C showed a slight but significant upward band shift relative to WT after oxidative treatment with potassium ferricyanide (K$_3$Fe(CN)$_6$) (Fig EV3B). Consistently, a Cβ-Cβ distance between T171 and L577 is 4.1 Å in the cryo-EM structure of SERCA2b in the E1·2Ca^{2+} state (Fig 5A). Additionally, it is predicted that two sulfur atoms of the introduced cysteines are located apart by a distance of 2.0 Å, and that a torsion angle of the Cβ–S–S–Cβ is +110° (Fig 5A, inset). These conditions are likely to meet the criteria for forming a disulfide bond between these two sites (Dombkowski et al, 2014).

Expectedly, purified T171C/L577C showed a significant upward band shift upon oxidation with K$_3$Fe(CN)$_6$, as compared to WT (Fig 5B). After treatment with dithiothreitol (DTT), T171C/L577C migrated at the same rate as WT (Fig 5B), suggesting the formation of a disulfide bond between the introduced cysteine residues in the A and N domains. Such an upward band shift caused by an interdomain disulfide bridge was previously observed for ERdj5, a protein disulfide isomerase (PDI) family member with an N-terminal J domain and six subsequent thioredoxin (Trx)-like domains (Maegawa et al, 2017).

Previous studies demonstrated that ATP can appropriately bind SERCA in the absence of Ca^{2+} to form E2-ATP state (Jensen et al, 2006; Kabashima et al, 2020). In this context, while the Cβ-Cβ distance between T171 and L577 is 9.9 Å in the crystal structure of SERCA1a in the E2 state (Toyoshima et al, 2013), it is reduced to 4.3 Å in the crystal structure of SERCA2a in the E2-AMPPCP state (Kabashima et al, 2020) (Fig EV4A). Using the same biochemical assay as above, we thus investigated if the closed headpiece cluster

of the cytosolic domains can be formed without Ca^{2+}. T171C/L577C was treated with 10 mM EGTA to generate the Ca^{2+}-free E2 state. Upon treatment with K$_3$Fe(CN)$_6$, the upper band (i.e., disulfide-bonded species) was slightly increased in intensity, but to a much lesser extent than in the presence of Ca^{2+} (i.e., without EGTA treatment) (Fig EV4B), suggesting that the A and N domains are located more separately from each other or fluctuate more largely in the Ca^{2+}-free E2 state. This observation seems consistent with the previous MD simulation starting from the "open-form" crystal structure of SERCA1a in the E1·2Ca^{2+} state, as this computational work demonstrated that the average simulated distance between the A and N domains in the final state is larger by 4.0 Å in the E2 state than in the E1 state, while the open-to-closed transition occurs more rapidly in the absence of Ca^{2+} (Espinoza-Fonseca & Thomas, 2011). We also added 1.5 mM AMPPCP (comparable to the physiological concentration of ATP) to T171C/L577C in order to examine the effect of ATP binding on the cytosolic domain arrangement. Unexpectedly, the disulfide-bonded species was not significantly increased by addition of AMPPCP in either the presence or absence of Ca^{2+} (Fig EV4B). Collectively, the results suggest that Ca^{2+} binding has greater effect on tight interaction between the A and N domains in SERCA than ATP binding. In agreement with this, the MD simulation showed that Ca^{2+} binding reshapes the free energy landscape of SERCA to create a path between the open and closed conformations (Espinoza-Fonseca & Thomas, 2011).

To explore the functional effect of the interdomain disulfide bond, we measured the ATPase activity of purified SERCA2b WT and T171C/L577C. The activity of T171C/L577C was almost abolished after treatment with K$_3$Fe(CN)$_6$, presumably because the interdomain disulfide bridge considerably constrained the cytosolic domain movements during the catalytic cycle (Fig 5C and D). In agreement with this, T171C/L577C largely restored the ATPase activity in the presence of DTT, up to the level comparable to WT. Unlike T171C/L577C, there was no substantial change in ATPase activity for WT following DTT or K$_3$Fe(CN)$_6$ treatment (Fig 5C and D). The different redox-reagent sensitivities of WT and T171C/L577C also support the formation of a disulfide bond between the A and N domains in T171C/L577C.

Using this mutant, we next performed an autophosphorylation assay with [γ-^{32}P] ATP to investigate whether the "closed-form" Ca^{2+}-bound SERCA2b could bind ATP at the appropriate site (Clausen et al, 2013; Chen et al, 2019). We first employed bovine serum albumin (BSA) as a negative control and confirmed no phosphorylation with this control (Fig EV4C). By contrast, SERCA2b WT displayed significant phosphorylation regardless of treatment with DTT and K$_3$Fe(CN)$_6$ (Fig 5E and F), indicating that these chemicals

Figure 3. **Conformational transition from the closed form of the E1·2Ca^{2+} state to the E1·2Ca^{2+}-ATP state.**

A Top view of the superposition of the A, N, and P domains between E1·2Ca^{2+} and E1·2Ca^{2+}-ATP states, in which all domains and TM helices are shown with transparency 0 (i.e., dense) for the E1·2Ca^{2+} state and 0.5 (i.e., faint) for the E1·2Ca^{2+}-ATP state. Cryo-EM structures of SERCA2b in E1·2Ca^{2+} and E1·2Ca^{2+}-ATP states are superimposed with each other such that the RMSD of all Cα atoms are minimized. The black and red arrows indicate ATP-induced movements of three β-strands and three α-helices contained in the C-terminal half of the P domain, respectively. The solid and dashed lines indicate the positions of these secondary structure elements before and after ATP binding, respectively. D351 indicated by spheres is a phosphorylation site.

B Superimposition of cryo-EM structures of SERCA2b in E1·2Ca^{2+} (yellow) and E1·2Ca^{2+}-ATP (cyan) states, in which TM7−TM10 are aligned with each other. The right inset shows a close-up view of the ATP-binding sites of SERCA2b in E1·2Ca^{2+} (yellow) and E1·2Ca^{2+}-AMPPCP (cyan) states, in which the two structures are superimposed such that the RMSD of their Cα atoms in the N domain is minimized. A Mg^{2+} ion close to AMPPCP is depicted as a green sphere. The lower inset highlights the side (left) and top (right) views of TM1−TM11 in E1·2Ca^{2+} (yellow) and E1·2Ca^{2+}-AMPPCP (cyan) states. The purple and cyan spheres indicate two bound Ca^{2+} ions in the E1·2Ca^{2+} and E1·2Ca^{2+}-ATP states, respectively.
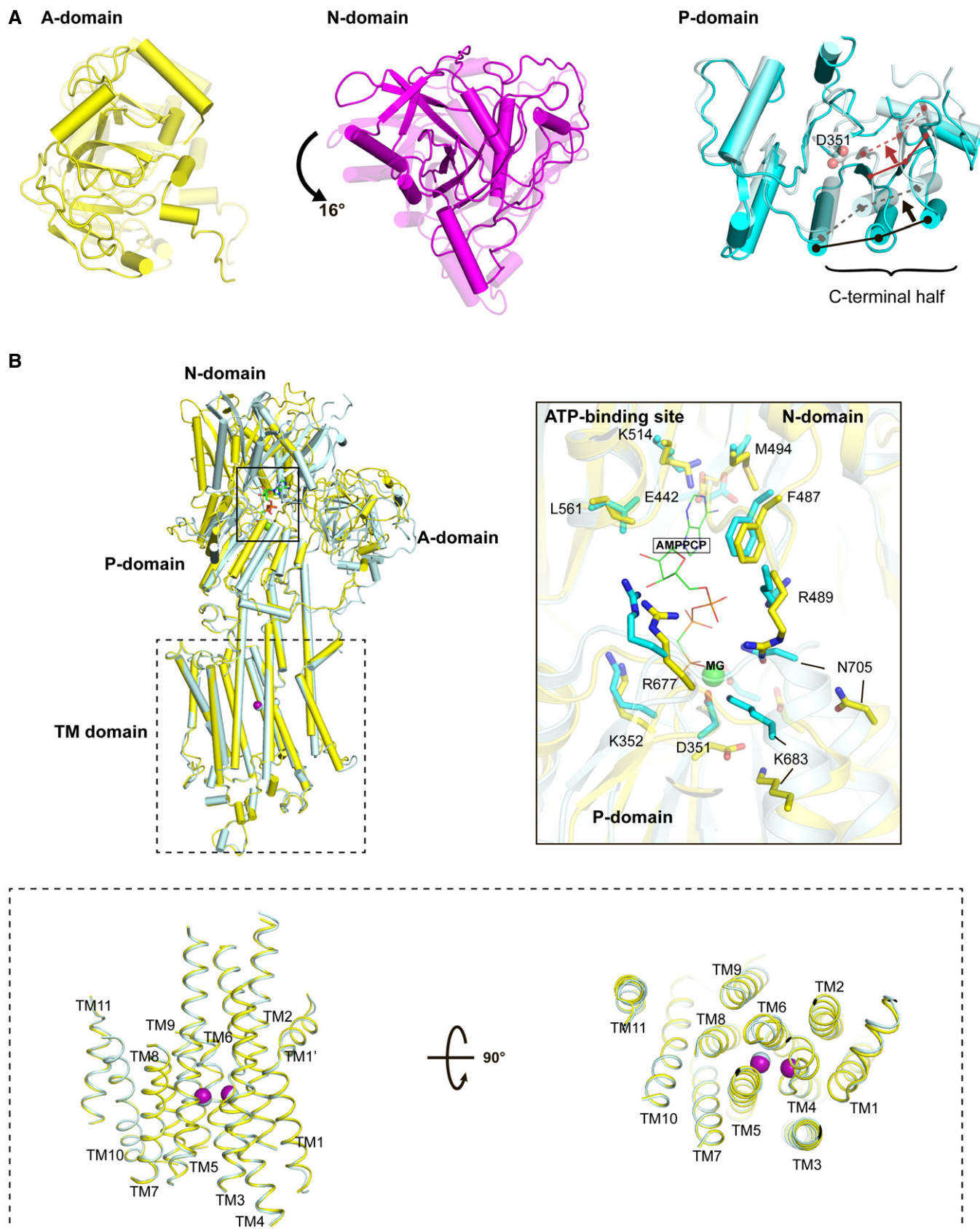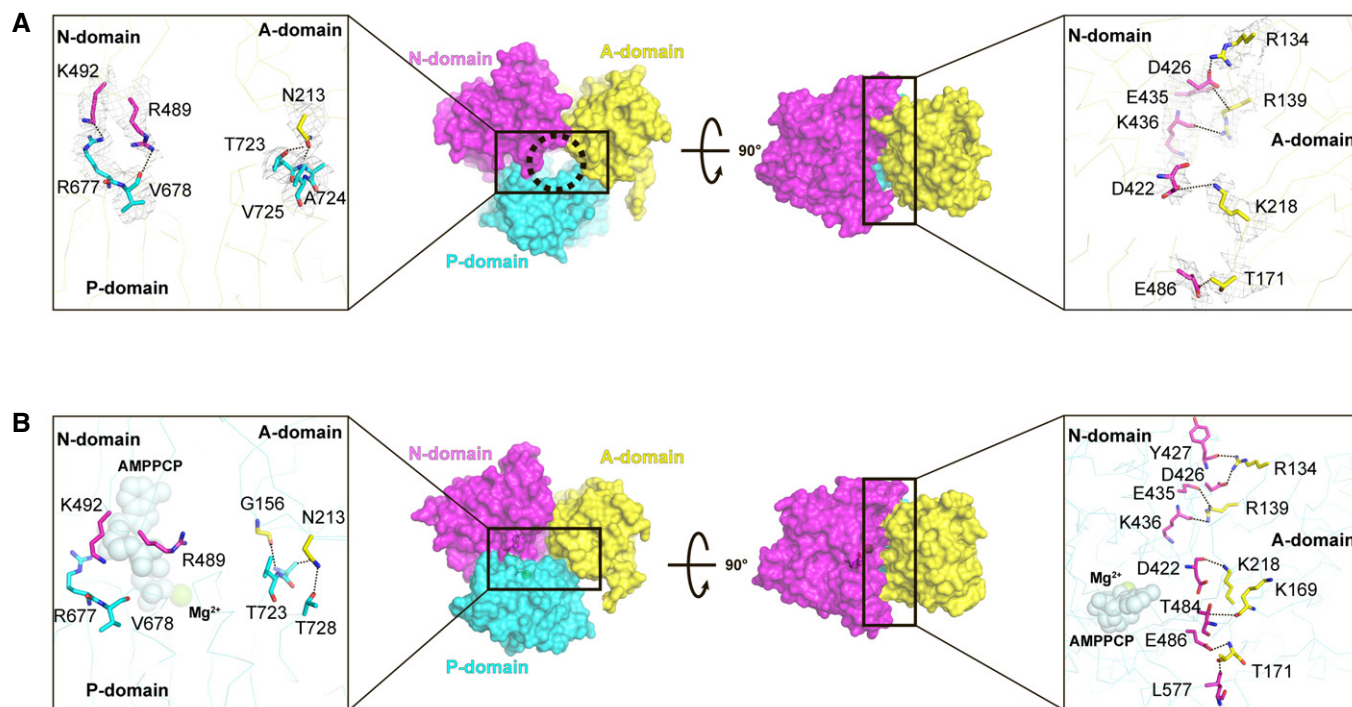
Figure 3.

Figure 4. Interface between the A and N domains in E1·2Ca²⁺ and E1·2Ca²⁺-AMPPCP states.

A Side (left) and top (right) views of the A, N, and P domains in the cryo-EM structure of SERCA2b in the E1·2Ca²⁺ state represented as a surface model. Residues critical for the domain interactions in the E1·2Ca²⁺ state are represented by sticks in the left and right insets. Gray mesh in the inset indicates the density of the resides shown at a contour level of 5.0 σ. The circle in the left panel indicates a cavity that may serve as an ATP entry gate in the "closed-form" SERCA2b.

B Side (left) and top (right) views of the A, N, and P domains in the cryo-EM structure of SERCA2b in the E1·2Ca²⁺-AMPPCP state shown in surface model representation. Residues critical for the domain interactions in the E1·2Ca²⁺-AMPPCP state are represented by sticks in the left and right insets. Dotted lines in the right inset indicate hydrogen bonds and salt bridges formed between the residues at the domain interface.

did not cause gross functional and structural changes to SERCA2b. Notably, T171C/L577C displayed significant phosphorylation even after treatment with $K_3Fe(CN)_6$, and its phosphorylated species displayed slower migration than those phosphorylated by WT (Fig 5E and F). After DTT treatment, the phosphorylated T171C/L577C species displayed the same electrophoretic mobility as WT (Fig 5E). Thus, the disulfide-bonded T171C/L577C mutant still retained autophosphorylation activity. Altogether, we conclude that an ATP molecule can enter the ATP-binding cavity formed in "closed-form" SERCA2b in the E1·2Ca²⁺ state, even without large cytosolic domain movements, and locate in a catalytically competent manner at the nucleotide-binding site to allow ATP hydrolysis.

Figure 5. Functional characterization of the "closed-form" SERCA2b.

A Close-up view of the interface between the A and N domains. The engineered site in the T171C/L577C mutant is highlighted in the inset.

B SDS–PAGE analysis of purified SERCA2b WT and T171C/L577C (0.5 μg each) after treatment with no reagent (−), 10 mM DTT, or 5 mM $K_3Fe(CN)_6$ at pH 7.0. Protein bands were visualized by staining with Coomassie Brilliant Blue. Note that T171C/L577C displayed a slower electrophoretic mobility than WT but displayed similar migration in the presence of DTT. "SS" and "no SS" indicate disulfide-bonded and non-disulfide-bonded SERCA2b species, respectively.

C ATPase activity of SERCA2b WT and T171C/L577C without reagents (−), or in the presence of DTT or $K_3Fe(CN)_6$. Results are means ± SD of three independent experiments.

D Bar graphs showing the relative ATPase activity of SERCA2b WT and T171C/L577C under the indicated conditions. Results are means ± standard deviation (SD) of three independent experiments. Relative absorbance at 360 nm is normalized with the absorbance of WT without reagents (−), and statistical significance is calculated by one-way ANOVA followed by Tukey's test. (ns, not significant; ****$P < 0.0001$).

E Autophosphorylation assays of SERCA2b WT and T171C/L577C without reagents (−), or in the presence of 10 mM DTT (+DTT) or 5 mM $K_3Fe(CN)_6$ (+$K_3Fe(CN)_6$). Protein bands were visualized by detecting ³²Pi with a Phosphorimager.

F Bar graphs showing the relative band intensity of ³²Pi-conjugated SERCA2b WT and T171C/L577C under the indicated conditions. Results are means ± SD of three independent experiments. Relative band intensity is normalized with the intensity of phosphorylated SERCA2b WT without reagents (−), and statistical significance is calculated by one-way ANOVA followed by Tukey's test. (ns, not significant).
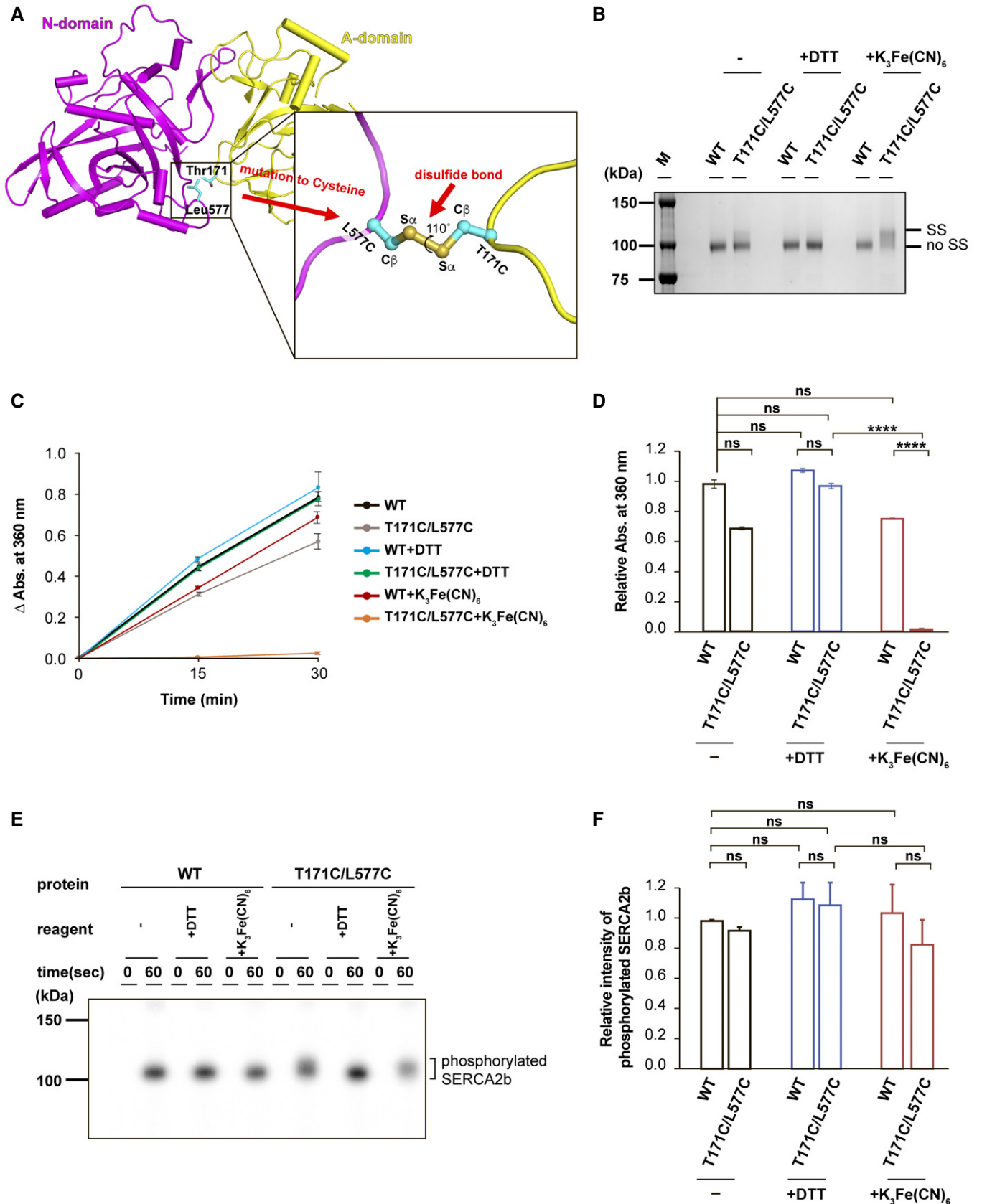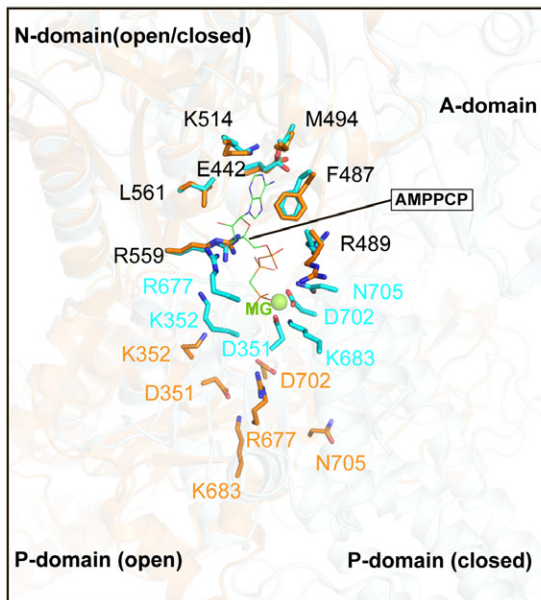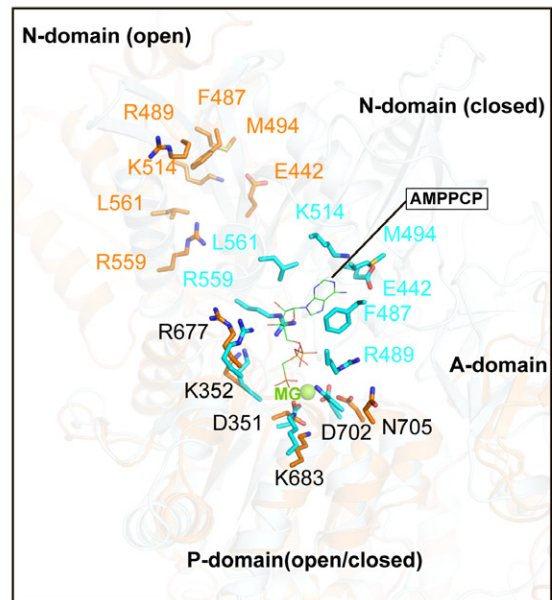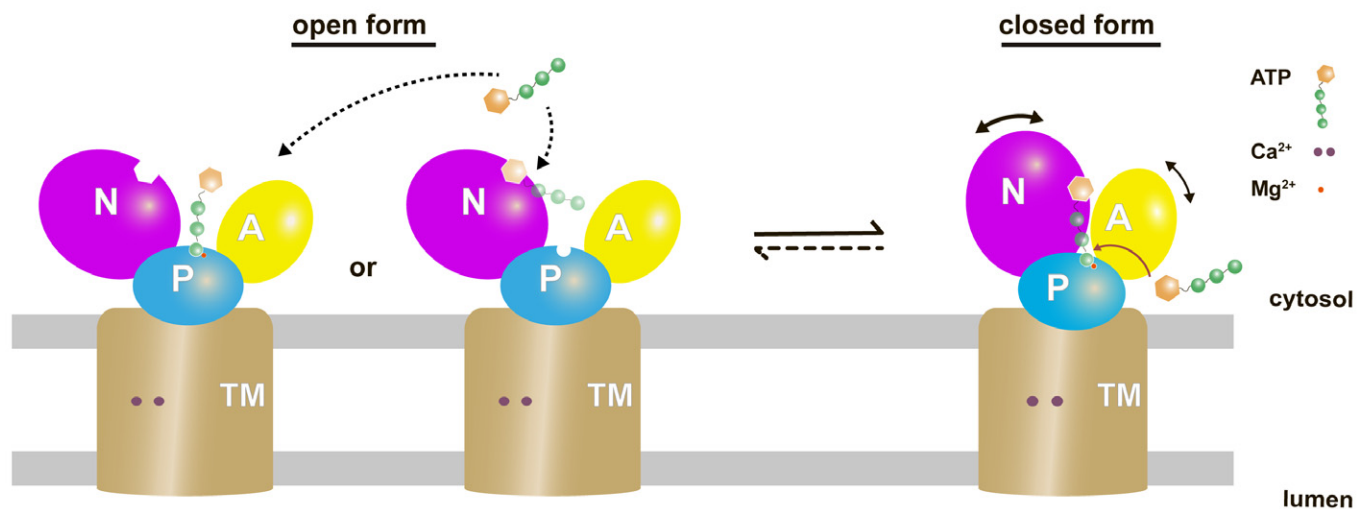
Figure 5.

Figure 6. Proposed mechanism of ATP binding to SERCA.

A Closed-up views of the ATP binding residues when the N domain (left) or the P domain (right) is superimposed between the cryo-EM structure of SERCA2b in the E1·2Ca^{2+}-AMPPCP state (cyan; PDB ID: 6LLE) and the "open-form" crystal structure of SERCA1a in the E1·2Ca^{2+} state (orange; PDB ID: 1SU4). The ATP binding residues in the former and the latter are represented by cyan and orange sticks, respectively. A Mg^{2+} ion close to the AMPPCP molecule is depicted as a green sphere. Note that all residues are numbered according to the residue number in SERCA2b.

B The present cryo-EM structure of SERCA2b in combination with the previous crystal structure of SERCA1a (PDB ID: 1SU4) reveals multiple conformations of SERCA in the E1·2Ca^{2+} state due to the highly mobile cytosolic domains, which could be in equilibrium between closed and open forms. While the open form largely exposes the ATP-binding site and therefore may readily receive and release ATP, the closed form appears to provide an ATP entry gate and serves as a preformed state immediately before ATP binding to SERCA.

Discussion

In the present cryo-EM single-particle analysis, multiple classes of conformations with different cytosolic domain arrangements were generated for SERCA2b in the E1·2Ca^{2+} state. The multiple

conformations could roughly be divided into "closed" and "possible open" forms (Fig EV1), consistent with the notion that the crystal structure of SERCA1a in the E1·2Ca^{2+} state represents only one structural aspect of the intermediate state (Liu & Barth, 2003). In line with this, open cytosolic domain conformations are not dominant among

the population of P-type ATPases (Dyla *et al*, 2019a), and several structures of the Ca^{2+}-free E1 intermediates of SERCA1a, including the crystal structure of SERCA1a in the $E1 \cdot Mg^{2+}$ state that is free from Ca^{2+} and ATP but binds a Mg^{2+} ion in the TM domain (Toyoshima, Iwasawa *et al*, 2013), have a more compact cytosolic domain arrangement than the "open-form" crystal structure of Ca^{2+}-bound SERCA1a (Akin *et al*, 2013; Toyoshima *et al*, 2013; Winther *et al*, 2013).

In the "open-form" crystal structure, several hydrogen bonds are formed between the A and P domains, contributing to stabilization of this domain arrangement (Fig EV3C, upper panel), while no interactions are made between the A and N domains (Fig EV3C, upper panel). The "closed-form" SERCA2b displays a completely different interdomain interaction pattern from the open form: The A domain makes contact with both the N and P domains via hydrogen bonds between different amino acid pairs (Fig EV3C, lower panel). Thus, modes of interaction among the A, N, and P domains are switched during the transition between open and closed forms, likely allowing multiple cytosolic domain arrangements in the $E1 \cdot 2Ca^{2+}$ state. In this context, previous computational and biophysical works demonstrated that the open cytosolic domain conformation is not predominant in either Ca^{2+}-bound or unbound state, but significantly more stabilized in the presence of Ca^{2+} (Winters *et al*, 2008; Espinoza-Fonseca & Thomas, 2011). The coexistence of the open and closed cytosolic domain arrangements in SERCA is reminiscent of different functional states of P-type ATPase Arabidopsis thaliana isoform 2 (AHA2) revealed by the single-molecule observation using total internal reflection fluorescence (TIRF) microscopy (Veshaguri *et al*, 2016). Proton pumping by AHA2 is stochastically interrupted by long-lived inactive or leaky states, and the active and inactive states together define the bulk activity. In this analogy, the open conformation in the $E1 \cdot 2Ca^{2+}$ state of SERCA may serve as a regulatory state that can pause the proper ATP binding and the subsequent hydrolysis in the catalytic cycle.

In this connection, it was previously proposed that an ATP molecule binds the open form and subsequently induces the large movement of the N domain, causing it to contact the A and P domains to form a compact cytosolic headpiece cluster (Toyoshima & Mizutani, 2004). Notably, detailed inspection between the ATP binding residues in the "open form" and the "ATP-bound form" provide mechanistic insight into ATP binding to SERCA (Fig 6A). Superimposition of the P or N domain between these two forms demonstrates that while the region responsible for contact with the adenosine moiety or the phosphate groups is individually preserved in the open form, simultaneous binding of these two parts of an ATP molecule seems impossible due to the far distant location of the P and N domains (Fig 6A). Therefore, even though the largely open cytosolic domain arrangement allows easy access of ATP to the well-exposed ATP-binding site, it will not ensure the tight or persistent ATP binding. By contrast, the "closed form" newly identified in this study places almost all ATP-binding residues at similar positions to those in the "ATP-bound form" (Fig 3B, right inset), suggesting that the ATP-binding pocket is preliminarily formed prior to ATP binding. Moreover, the "closed form" of SERCA2b appears to form a cavity that may serve as an ATP entry gate (Fig 4A). In support of this, the T171C/L577C mutant that constitutively maintains the closed form could bind and hydrolyze ATP to a significant extent (Fig 5).

Given the millimolar levels of intracellular ATP, seemingly high enough to saturate SERCA throughout the catalytic cycle, Ca^{2+} binding is likely coordinated to ATP binding. In other words, the E2-ATP state could predominantly exist to efficiently incorporate Ca^{2+} under physiological conditions. Although both biochemical and computational works demonstrate that SERCA is incapable of hydrolyzing ATP without bound Ca^{2+} (Inesi *et al*, 2006; Das *et al*, 2017; Thirman *et al*, 2021), ATP molecule can be properly delivered to the binding pocket regardless of the availability of Ca^{2+} (Jensen *et al*, 2006; Kabashima *et al*, 2020). Nevertheless, the ATP-unbound E1 state may possibly be generated in some particular local or transient environments where ADP and Ca^{2+} are highly abundant. SERCA2b has been reported to be enriched in the mitochondria-associated ER-membrane (MAM) and play an important role in Ca^{2+} signaling and homeostasis between the ER and the mitochondria (Lynes *et al*, 2013; Xiao *et al*, 2017). It is also known that IP3 receptor, a primary actor in Ca^{2+} efflux from the ER lumen, is situated at the ER–mitochondria interface to transport Ca^{2+} to the mitochondria in concert with GRp75, and VDAC1 (Szabadkai & Bianchi, 2006; Patergnani *et al*, 2011). In this regard, it will be interesting to investigate the precise concentrations of Ca^{2+} and ATP/ADP in the MAM compartment and their possible variations caused by the chemical crosstalk between these two organelles.

In conclusion, the closed form with less mobile cytosolic domains can allow an ATP molecule to appropriately enter the ATP-binding cavity and drive ATP hydrolysis (Fig 6B, right). Although we cannot exclude a possibility that SERCA2b in the $E1 \cdot 2Ca^{2+}$ state is in equilibrium between the open and closed forms and that the open form binds ATP and subsequently adopts the $E1 \cdot 2Ca^{2+}$-ATP state, the present study demonstrated that the closed form can do so even without returning to the open form via large cytosolic domain movements. Our findings provide a framework for further understanding the mechanism of ATP entry to SERCA Ca^{2+}-ATPase during its Ca^{2+} transport cycle.

Materials and Methods

Expression of human PA-SERCA2b WT and T171C/L577C mutant

Expression of SERCA2b WT was carried out as described previously (Inoue *et al*, 2019; Zhang *et al*, 2020). In brief, a PiggyBac Cumate Switch-Inducible Vector harboring an open reading frame encoding human SERCA2b WT was introduced into HEK293T cells along with a Super PiggyBac Transposase Expression Vector (System Bioscience, LLC, CA, USA), using polyethylenimine (Sigma-Aldrich) to generate a stable cell line for overexpression of each protein. Cells were grown in Dulbecco's modified Eagle's medium with 4% inactivated fetal calf serum and incubated in a humidified incubator with 5% CO_2 at 37°C. After 2 days of incubation, the expression of SERCA2b WT or T1032stop was induced with cumate (150 μg/ml) and phorbol 12-myristate 13-acetate (50 ng/ml). Cells were incubated at 37°C for another 48 h and then harvested by centrifugation at 1,000 *g* for 15 min.

The SERCA2b mutants were prepared by site-directed mutagenesis using the plasmid pcDNA3.1/PA-SERCA2b as a template, and primers 5′-ggacagaaagagtgtgtgccggattaaagc-3′, 5′-gtctttagctttaatccgg cacacactctttc-3′, 5′-ctttgtaatgactctgctttgtgctacaatgaggc-3′, and 5′-cccctt tgcctcattgtagcacaaagcagagtc-3′ for Q138C/D426C; primers 5′- ggacag aaagagttgccagcggattaaagc-3′, 5′-gtctttagctttaatccgctggcaactctttctg-3′, 5′-ctttgtaatgactctgctttgtgctacaatgaggc-3′, and 5′-cccctttgcctcattgtagca

caaagcagagtc-3′ for V137C/D426C; primers 5′-gaaatttgcgttggtgacaaag ttcctgc-3′, 5′-caccaacgcaaatttctacaatatcaccagg-3′, 5′-gaaaaagtttgcgaag ctacagagagactgctc-3′, and 5′-gtagcttcgcaaacttttttcatacacaccc-3′ for A154C/G438C; primers 5′-gaaattgcttgcggtgacaaaagttcctgc-3′, 5′-caccgc aagcaatttctacaatatcaccagg-3′, 5′-gaaaaagtttgcgaagctacagagagactgctc-3′, and 5′-gtagcttcgcaaactttttcatacacaccc-3′ for V155C/G438C; and primers 5′-ccatcaaatcttgcacactaagagttgacc-3′, 5′-ctcttagtgtgcaagatttg atggaagttaacc-3′, 5′-ggaattcactctatgctttttcacgtgacagaaag-3′, and 5′-cgtg aaaagcatagagtgaattcctttttcatc-3′ for T171C/E486C; and primers 5′-g aaattgcttgcggtgacaaagttcctgc-3′, 5′-caccgcaagcaatttctacaatatcaccagg-3′, 5′-gaaatgcactgcgaggactctgccaac-3′, and 5′-gtcctcgcagtgcatttcttctc ttctcag-3′ for T1171C/L577C. The mutant was expressed in the same way as SERCA2b WT.

Purification of SERCA2b WT and T171C/L577C mutant

The purification procedures were performed as described previously (Inoue *et al*, 2019; Zhang *et al*, 2020). Briefly, cells were lysed using a Dounce homogenizer and solubilized in buffer containing 50 mM HEPES-NaOH (pH 7.0), 100 mM NaCl, 20% glycerol, 1 mM $CaCl_2$, 1 mM $MgCl_2$, 1 mM dithiothreitol (DTT), 1 mM phenylmethylsulfonyl fluoride, and 1/100 Protease Inhibitor Cocktail (Nacalai). After homogenization, 1% (w/v) n-dodecyl-β-D-maltoside (DDM) was added to solubilize the membrane fraction. The sample was centrifuged at 20,100 *g* for 1.5 h to remove insoluble material after gentle rotation. The supernatant was collected and incubated overnight with anti-PA sepharose beads. Ten column volumes of buffer containing 50 mM HEPES-NaOH (pH 7.0), 100 mM KCl, 20% glycerol, 1 mM $CaCl_2$, 1 mM $MgCl_2$, 1 mM DTT, and 0.05% (w/v) lauryl maltose neopentyl glycol (LMNG) were used to wash beads, followed by elution with the same buffer containing 0.2 mg/ml PA peptide. Eluted fractions were concentrated to 0.5 ml and further purified by size-exclusion chromatography (SEC) on a Superose 6 10/300 GL column (GE Healthcare) with the same buffer. Peak fractions were concentrated to 10 mg/ml with an Amicon filter device equipped with a 100 kDa cutoff membrane.

For functional assays, SERCA2b WT and T171C/L577C were purified using the same protocols described in grid preparation for cryo-EM measurement, except that no DTT was added to the buffer.

Autophosphorylation assay

Autophosphorylation of purified PA-tagged SERCA2b WT and T171C/L577C was carried out using [γ-^{32}P] ATP essentially as described previously (Clausen *et al*, 2013; Chen *et al*, 2019). Briefly, the reaction mixture contained 0.5 μg of purified PA-SERCA2b or 40 μg of BSA in buffer containing 100 mM KCl, 50 mM HEPES-NaOH (pH 7.0), 20% glycerol, 1 mM $CaCl_2$, 1 mM $MgCl_2$, and 0.01% (w/v) LMNG, following treatment with 10 mM DTT or 5 mM $K_3Fe(CN)_6$. The reaction was initiated by addition of 0.074 MBq of [γ-^{32}P] ATP (PerkinElmer Life Sciences) at a final concentration of 5 μM. After a 60-s reaction at 25°C, acid quenching of the phosphorylated enzyme was performed with 50 μl stop solution containing 10% trichloroacetic acid (TCA) and 50 mM phosphoric acid (H_3PO_4). For a 0-s control reaction, the stop solution was first mixed with the radioisotope solution. Then, pre-incubated SERCA2b WT or T171C/L577C mutant was added. The protein pellet was collected by centrifugation, washed with 100% acetone,

and subjected to SDS–PAGE on a 7.5% polyacrylamide gel at pH 6.0 (Clausen *et al*, 2013; Chen *et al*, 2019). The radioactive bands were detected using a BAS IP MS 2040 E imaging plate (GE Healthcare) and an FLA-2000 Phosphorimager (Fuji Film). The radioactive band was quantified by ImageJ.

ATPase activity assay

The ATPase activities of purified SERCA2b WT and T171C/L577C were measured as described previously (Ushioda *et al*, 2016; Inoue *et al*, 2019). Briefly, purified SERCA2b WT or T171C/L577C mutant in buffer containing 50 mM HEPES-NaOH (pH 7.0), 100 mM KCl, 20% glycerol, 1 mM $MgCl_2$, and 10 μM $CaCl_2$ was treated with or without 10 mM DTT. ATP (1 mM) was then added and incubated at 37°C for 10 min to start the SERCA ATPase reaction cycle. The reaction was stopped using 5 mM EDTA, and the resultant solution was treated with an EnzCheck phosphate assay kit (Thermo Fisher Scientific). The mixture was incubated at 22°C for 30 min, and the absorbance at 360 nm was measured with a U-3900 Spectrophotometer (Hitachi).

Grid preparation for cryo-EM

To prepare the E1·2Ca^{2+} form, a second round of SEC was performed on the same column at 4°C with 50 mM HEPES-NaOH (pH 7.0), 100 mM KCl, 0% glycerol, 1 mM $CaCl_2$, 1 mM $MgCl_2$, 1 mM DTT, and 0.01% (w/v) LMNG to remove glycerol and decrease the detergent concentration. The peak fractions were collected and concentrated to 4−8 mg/ml for cryo-EM measurement. Grid preparation was the same as described previously. Briefly, purified samples (2−3 μl) were applied to a freshly glow-discharged 300 mesh Quantifoil 1.2/1.3 carbon grid using Vitrobot (Thermo Fisher Scientific) with a blotting time of 3−4 s under 100% humidity at 4°C, and grids were plunge-frozen in liquid ethane.

Cryo-EM data collection and image processing

Prepared grids were transferred to a Titan Krios G3i microscope (Thermo Fisher Scientific), which was operated at 300 kV and equipped with a Gatan Quantum-LS Energy Filter (GIF) with a slit width of 25 eV and a Gatan K3 Summit direct electron detector in the electron counting mode. Imaging was performed at a nominal magnification of ×105,000, corresponding to a calibrated pixel size of 0.83 Å per pixel (University of Tokyo, Japan). Each movie was recorded for 3 s and subdivided into 60 frames. The electron flux was set to 14 e⁻/pixel/s at the detector, resulting in an accumulated exposure of 60 e⁻/Å² at the specimen. Data were automatically acquired by the image shift method using SerialEM software (Mastronarde, 2005), with a 3 × 3 beam-image shift (BIS) pattern and a defocus range of −0.8 to −1.8 μm. In total, 3,555 movies were acquired for the grid, and the precise number of images is described in Table EV1. For the dataset, dose-fractionated movies were subjected to beam-induced motion correction using Relion-3 (Zivanov *et al*, 2018), and contrast transfer function (CTF) parameters were estimated using CTFFIND4 (Rohou & Grigorieff, 2015).

Particles were extracted from motion-corrected micrographs with down-sampling to a pixel size of 3.32 Å per pixel. These particles

were subjected to three rounds of 2D classification using the number of classes k = 100 and a tau-fudge value of 2, followed by two rounds of 3D classification using the number of classes k = 4 and a tau-fudge value of 4 by RELION 3.1 (Zivanov *et al*, 2018). Meanwhile, quick data assessment with 2D classification, ab initio reconstruction, heterogeneous refinement, and non-uniform refinement by cryoSPARC v2.14 (Punjani *et al*, 2017) was performed to produce a 3D initial model, which was used as a reference for the 3D classification by RELION 3.1. The best particles were selected, re-extracted with a pixel size of 1.245 Å per pixel, and subjected to auto-3D refinement. The resulting 3D maps and particle sets were subjected to per-particle defocus refinement, beam-tilt refinement, Bayesian polishing, second per-particle defocus refinement, and 3D refinement. An additional 3D classification was performed without masking for "closed-form" SERCA2b. The global resolution of SERCA2b WT in the E1·2Ca^{2+} state was 3.3 Å. The resolution was calculated according to the Fourier Shell Correlation (FSC) = 0.143 criterion (Rosenthal & Henderson, 2003). The local resolution was estimated using RELION 3.1 (Zivanov *et al*, 2018). Detailed processing strategies are shown in Fig EV1.

Model building, refinement, and validation

The cryo-EM structure of SERCA2b WT in the E1·2Ca^{2+} state was modeled using cryo-EM structures of human SERCA2b WT in the AMPPCP state (PDB ID: 6LLE) as an initial model. After rigid-body fitting of each cytosolic domain in PHENIX (Adam-Vizi & Starkov, 2010; Afonine *et al*, 2018), a structure model was further refined manually and iteratively using Coot (Emsley & Cowtan, 2004), and then, several rounds of structure refinement were carried out using "phenix.real_space_refine" in PHENIX with secondary structure restraint. The geometry of the structure model was validated using MolProbity (Chen *et al*, 2010). All the structural figures were prepared in UCSF Chimera (Pettersen *et al*, 2004) and PyMOL (https://pymol.org/2/). The linker regions composed of residues 505−506, and 993–1,012, which were located at L1/2, the N domain, and L10/11, respectively, could not be modeled due to missing and disordered density in the cryo-EM map. The statistics for 3D reconstitution and model refinement are summarized in Table EV1.

Statistical analysis

Results of gel images, ATPase activity, and autoradiography are shown as mean ± SD of three independent experiments. All statistical significance was calculated by one-way ANOVA followed by Tukey's test and indicated by asterisks: $*P < 0.05$; $**P < 0.005$.

Data availability

All data needed to evaluate the conclusions in the paper are included in the paper and/or the Supplementary Materials. Additional data supporting the findings of this manuscript are available from the corresponding authors upon reasonable request. Atomic coordinates of human SERCA2b in the E1·2Ca^{2+} state have been deposited in the Protein Data Bank (https://pdbj.org/) under accession codes 7E7S. The cryo-EM density map has been deposited in

the Electron Microscopy Data Bank (https://www.ebi.ac.uk/pdbe/emdb/) under accession codes EMD-31003.

Author contributions
YZ performed almost all experiments, structure modeling, and structure refinement. AT and MK performed acquisition of cryo-EM image data. SW assisted in structure modeling and refinement. HK assisted in autophosphorylation experiments with [γ-^{32}P] ATP. YZ and KI prepared figures and wrote the manuscript. All authors discussed the results, critically read the manuscript, and approved the manuscript for submission. KI supervised this work.

Conflict of interest
The authors declare that they have no conflict of interest.

References

Adam-Vizi V, Starkov AA (2010) Calcium and mitochondrial reactive oxygen species generation: how to read the facts. *J Alzheimers Dis* 20: S413−S426

Afonine PV, Poon BK, Read RJ, Sobolev OV, Terwilliger TC, Urzhumtsev A, Adams PD (2018) Real-space refinement in PHENIX for cryo-EM and crystallography. *Acta Crystallogr D Struct Biol* 74: 531−544

Akin BL, Hurley TD, Chen Z, Jones LR (2013) The structural basis for phospholamban inhibition of the calcium pump in sarcoplasmic reticulum. *J Biol Chem* 288: 30181−30191

Axelsen KB, Palmgren MG (1998) Evolution of substrate specificities in the P-type ATPase superfamily. *J Mol Evol* 46: 84−101

Bublitz M, Musgaard M, Poulsen H, Thøgersen L, Olesen C, Schiøtt B, Morth JP, Møller JV, Nissen P (2013) Ion pathways in the sarcoplasmic reticulum Ca2+-ATPase. *J Biol Chem* 288: 10759−10765

Bublitz M, Poulsen H, Morth JP, Nissen P (2010) In and out of the cation pumps: P-type ATPase structure revisited. *Curr Opin Struct Biol* 20: 431−439

Chen J, Smaardijk S, Mattelaer C-A, Pamula F, Vandecaetsbeek I, Vanoevelen J, Wuytack F, Lescrinier E, Eggermont J, Vangheluwe P (2019) An N-terminal Ca2+-binding motif regulates the secretory pathway Ca2+/Mn2+-transport ATPase SPCA1. *J Biol Chem* 294: 7878−7891

Chen VB, Arendall WB, Headd JJ, Keedy DA, Immormino RM, Kapral GJ, Murray LW, Richardson JS, Richardson DC (2010) MolProbity: all-atom structure validation for macromolecular crystallography. *Acta Crystallogr D Biol Crystallogr* 66: 12−21

Clausen JD, Bublitz M, Arnou B, Montigny C, Jaxel C, Møller JV, Nissen P, Andersen JP, Le Maire M (2013) SERCA mutant E309Q binds two Ca2+ ions but adopts a catalytically incompetent conformation. *EMBO J* 32: 3231−3243

Das A, Gur M, Cheng MH, Jo S, Bahar I, Roux B (2014) Exploring the conformational transitions of biomolecular systems using a simple two-state anisotropic network model. *PLoS Comput Biol* 10: e1003521

Das A, Rui H, Nakamoto R, Roux B (2017) Conformational transitions and alternating-access mechanism in the sarcoplasmic reticulum calcium pump. *J Mol Biol* 429: 647–666

Dombkowski AA, Sultana KZ, Craig DB (2014) Protein disulfide engineering. *FEBS Lett* 588: 206–212

Dyla M, Basse Hansen S, Nissen P, Kjaergaard M (2019a) Structural dynamics of P-type ATPase ion pumps. *Biochem Soc Trans* 47: 1247–1257

Dyla M, Kjærgaard M, Poulsen H, Nissen P (2019b) Structure and Mechanism of P-Type ATPase Ion Pumps. *Annu Rev Biochem* 89: 583–603

Dyla M, Terry DS, Kjaergaard M, Sørensen TL-M, Andersen JL, Andersen JP, Knudsen CR, Altman RB, Nissen P, Blanchard SC (2017) Dynamics of P-type ATPase transport revealed by single-molecule FRET. *Nature* 551: 346–351

Emsley P, Cowtan K (2004) Coot: model-building tools for molecular graphics. *Acta Crystallogr D Biol Crystallogr* 60: 2126–2132

Espinoza-Fonseca LM, Thomas DD (2011) Atomic-level characterization of the activation mechanism of SERCA by calcium. *PLoS One* 6: e26936

Focht D, Croll TI, Pedersen BP, Nissen P (2017) Improved model of proton pump crystal structure obtained by interactive molecular dynamics flexible fitting expands the mechanistic model for proton translocation in P-Type ATPases. *Front Physiol* 8: 202

Hiraizumi M, Yamashita K, Nishizawa T, Nureki O (2019) Cryo-EM structures capture the transport cycle of the P4-ATPase flippase. *Science* 365: 1149–1155

Huang Y, Li H, Bu Y (2009) Molecular dynamics simulation exploration of cooperative migration mechanism of calcium ions in sarcoplasmic reticulum Ca2+-ATPase. *J Comput Chem* 30: 2136–2145

Inesi G, Lewis D, Ma H, Prasad A, Toyoshima C (2006) Concerted conformational effects of Ca2+ and ATP are required for activation of sequential reactions in the Ca2+ ATPase (SERCA) catalytic cycle. *Biochemistry* 45: 13769–13778

Inoue M, Sakuta N, Watanabe S, Zhang Y, Yoshikaie K, Tanaka Y, Ushioda R, Kato Y, Takagi J, Tsukazaki T *et al* (2019) Structural basis of Sarco/endoplasmic reticulum Ca2+-ATPase 2b regulation via transmembrane helix interplay. *Cell Rep* 27: 1221–1230.e3

Jensen AML, Sørensen TLM, Olesen C, Møller JV, Nissen P (2006) Modulatory and catalytic modes of ATP binding by the calcium pump. *EMBO J* 25: 2305–2314

Kabashima Y, Ogawa H, Nakajima R, Toyoshima C (2020) What ATP binding does to the Ca2+ pump and how nonproductive phosphoryl transfer is prevented in the absence of Ca2+. *Proc Natl Acad Sci USA* 117: 18448–18458

Kekenes-Huskey PM, Metzger VT, Grant BJ, Andrew McCammon J (2012) Calcium binding and allosteric signaling mechanisms for the sarcoplasmic reticulum Ca2+ ATPase. *Protein Sci* 21: 1429–1443

Liu M, Barth A (2003) Mapping interactions between the Ca2+-ATPase and its substrate ATP with infrared spectroscopy. *J Biol Chem* 278: 10112–10118

Lopez-Redondo ML, Coudray N, Zhang Z, Alexopoulos J, Stokes DL (2018) Structural basis for the alternating access mechanism of the cation diffusion facilitator YiiP. *Proc Natl Acad Sci USA* 115: 3042–3047

Lynes EM, Raturi A, Shenkman M, Sandoval CO, Yap MC, Wu J, Janowicz A, Myhill N, Benson MD, Campbell RE (2013) Palmitoylation is the switch that assigns calnexin to quality control or ER Ca2+ signaling. *J Cell Sci* 126: 3893–3903

Maegawa K-I, Watanabe S, Noi K, Okumura M, Amagai Y, Inoue M, Ushioda R, Nagata K, Ogura T, Inaba K (2017) The highly dynamic nature of ERdj5 is key to efficient elimination of aberrant protein oligomers through ER-associated degradation. *Structure* 25: 846–857.e4

Mastronarde DN (2005) Automated electron microscope tomography using robust prediction of specimen movements. *J Struct Biol* 152: 36–51

Michelangeli F, East JM (2011) A diversity of SERCA Ca2+ pump inhibitors. *Biochem Soc Trans* 39: 789–797

Møller JV, Nissen P, Sørensen TL, le Maire M (2005) Transport mechanism of the sarcoplasmic reticulum Ca2+-ATPase pump. *Curr Opin Struct Biol* 15: 387–393

Møller JV, Olesen C, Winther A-ML, Nissen P (2010) The sarcoplasmic Ca2+-ATPase: design of a perfect chemi-osmotic pump. *Q Rev Biophys* 43: 501

Morth JP, Pedersen BP, Toustrup-Jensen MS, Sørensen TL-M, Petersen J, Andersen JP, Vilsen B, Nissen P (2007) Crystal structure of the sodium–potassium pump. *Nature* 450: 1043–1049

Mueller B, Zhao M, Negrashov IV, Bennett R, Thomas DD (2004) SERCA structural dynamics induced by ATP and calcium. *Biochemistry* 43: 12846–12854

Nyblom M, Poulsen H, Gourdon P, Reinhard L, Andersson M, Lindahl E, Fedosova N, Nissen P (2013) Crystal structure of Na$^+$, K$^+$-ATPase in the Na$^+$-bound state. *Science* 342: 123–127

Patergnani S, Suski JM, Agnoletto C, Bononi A, Bonora M, De Marchi E, Giorgi C, Marchi S, Missiroli S, Poletti F *et al* (2011) Calcium signaling around mitochondria associated membranes (MAMs). *Cell Commun Signal* 9: 1–10

Pettersen EF, Goddard TD, Huang CC, Couch GS, Greenblatt DM, Meng EC, Ferrin TE (2004) UCSF Chimera—a visualization system for exploratory research and analysis. *J Comput Chem* 25: 1605–1612

Punjani A, Rubinstein JL, Fleet DJ, Brubaker MA (2017) cryoSPARC: algorithms for rapid unsupervised cryo-EM structure determination. *Nat Methods* 14: 290–296

Raguimova ON, Smolin N, Bovo E, Bhayani S, Autry JM, Zima AV, Robia SL (2018) Redistribution of SERCA calcium pump conformers during intracellular calcium signaling. *J Biol Chem* 293: 10843–10856

Ravishankar H, Pedersen MN, Eklund M, Sitsel A, Li C, Duelli A, Levantino M, Wulff M, Barth A, Olesen C (2020) Tracking Ca2+ ATPase intermediates in real time by x-ray solution scattering. Science. *Advances* 6: eaaz0981

Rohou A, Grigorieff N (2015) CTFFIND4: Fast and accurate defocus estimation from electron micrographs. *J Struct Biol* 192: 216–221

Rosenthal PB, Henderson R (2003) Optimal determination of particle orientation, absolute hand, and contrast loss in single-particle electron cry microscopy. *J Mol Biol* 333: 721–745

Szabadkai G, Bianchi K, Várnai P, Destefani D, Wieckowski MR, Cavagna D, Nagy AI, Balla T, Rizzuto R (2006) Chaperone-mediated coupling of endoplasmic reticulum and mitochondrial Ca2+ channels. *J Cell Biol* 175: 901–911.

Thirman J, Rui H, Roux B (2021) Elusive intermediate state key in the conversion of ATP hydrolysis into useful work driving the Ca2+ pump SERCA. *J Phys Chem B* 125: 2921–2928

Timcenko M, Lyons JA, Januliene D, Ulstrup JJ, Dieudonné T, Montigny C, Ash M-R, Karlsen JL, Boesen T, Kühlbrandt W *et al* (2019) Structure and autoregulation of a P4-ATPase lipid flippase. *Nature* 571: 366–370

Toyoshima C (2009) How Ca2+-ATPase pumps ions across the sarcoplasmic reticulum membrane. *Biochim Biophys Acta Mol Cell Res* 1793: 941–946

Toyoshima C, Iwasawa S, Ogawa H, Hirata A, Tsueda J, Inesi G (2013) Crystal structures of the calcium pump and sarcolipin in the Mg 2+-bound E1 state. *Nature* 495: 260–264

Toyoshima C, Mizutani T (2004) Crystal structure of the calcium pump with a bound ATP analogue. *Nature* 430: 529–535

Toyoshima C, Nakasako M, Nomura H, Ogawa H (2000) Crystal structure of the calcium pump of sarcoplasmic reticulum at 2.6 Å resolution. *Nature* 405: 647–655

Ushioda R, Miyamoto A, Inoue M, Watanabe S, Okumura M, Maegawa K-I, Uegaki K, Fujii S, Fukuda Y, Umitsu M (2016) Redox-assisted regulation of Ca2+ homeostasis in the endoplasmic reticulum by disulfide reductase ERdj5. *Proc Natl Acad Sci USA* 113: E6055–E6063

Veshaguri S, Christensen SM, Kemmer GC, Ghale G, Moller MP, Lohr C, Christensen AL, Justesen BH, Jorgensen IL, Schiller J *et al* (2016) Direct observation of proton pumping by a eukaryotic P-type ATPase. *Science* 351: 1469–1473

Winters DL, Autry JM, Svensson B, Thomas DD (2008) Interdomain fluorescence resonance energy transfer in SERCA probed by cyan-fluorescent protein fused to the actuator domain. *Biochemistry* 47: 4246–4256

Winther A-ML, Bublitz M, Karlsen JL, Møller JV, Hansen JB, Nissen P, Buch-Pedersen MJ (2013) The sarcolipin-bound calcium pump stabilizes calcium sites exposed to the cytoplasm. *Nature* 495: 265–269

Xiao F, Zhang J, Zhang C, An W (2017) Hepatic stimulator substance inhibits calcium overflow through the mitochondria-associated membrane compartment during nonalcoholic steatohepatitis. *Lab Invest* 97: 289–301

Zhang Y, Fujii J, Phillips MS, Chen H-S, Karpati G, Yee W-C, Schrank B, Cornblath DR, Boylan KB, MacLennan DH (1995) Characterization of cDNA and genomic DNA encoding SERCA1, the Ca2+-ATPase of human fast-twitch skeletal muscle sarcoplasmic reticulum, and its elimination as a candidate gene for Brody disease. *Genomics* 30: 415–424

Zhang Y, Inoue M, Tsutsumi A, Watanabe S, Nishizawa T, Nagata K, Kikkawa M, Inaba K (2020) Cryo-EM structures of SERCA2b reveal the mechanism of regulation by the luminal extension tail. *Sci Adv* 6: eabb0147

Zivanov J, Nakane T, Forsberg BO, Kimanius D, Hagen WJ, Lindahl E, Scheres SH (2018) New tools for automated high-resolution cryo-EM structure determination in RELION-3. *Elife* 7: e42166